IEEE Access
Multidisciplinary | Rapid Review | Open Access Journal

Received May 8, 2021, accepted May 23, 2021, date of publication May 28, 2021, date of current version June 21, 2021.

Digital Object Identifier 10.1109/ACCESS.2021.3084630

Small Signal Modelling for Variable Frequency Control With Maximum Efficiency Point Tracking of DAB Converter

IVAN RUIZ ERNI, (Graduate Student Member, IEEE), ENRIC VIDAL-IDIARTE, (Member, IEEE), JAVIER CALVENTE, (Member, IEEE), AND LUIS GUASCH-PESQUER

Departament d'Enginyeria Electrònica, Elèctrica i Automàtica, Universitat Rovira i Virgili, 43007 Tarrangona, Spain

Corresponding authors: Ivan Ruiz Erni (ivanr@ieee.org) and Enric Vidal-Idiarte (enric.vidal@urv.cat)

This work was supported in part by the Universitat Rovira i Virgili under Project URV SGR2017 00983.

ABSTRACT Dual active bridge (DAB) converters have experienced a boom thanks to the demands of new applications where bidirectional energy transfer, galvanic isolation and high efficiency are essential. In order to improve the efficiency of the stage without losing sight of the converter advantages, previous works have proposed complex forms of control that are not always applicable. This paper proposes the use of a variable frequency control strategy plus an additional control loop to find the point of maximum efficiency. Therefore, in this paper, the generalized state space average model is developed in depth to obtain in an analytical way a new small-signal model between the switching frequency and the output voltage, which is used to design the digital variable frequency control. In addition, to increase efficiency, reduce losses and ensure zero voltage switching, a second loop based on perturb and observe methodology is presented. The results obtained in the analysis of this control are validated and contrasted by simulation and experimentally with a 1kW prototype.

INDEX TERMS Dual active bridge, digital control, GSSAM.

I. INTRODUCTION

Isolated and bidirectional DC-DC converters are becoming more popular thanks to new market opportunities. The interest in the application of the non resonant dual active bridge (DAB) for isolated DC-DC power conversion systems has been continuously growing [1], [2]. Its easy soft-switching realization, bidirectional power transfer capability, and modular and symmetrical structure made it a good candidate in automotive application [3]–[7], fuel-cell and battery storage systems [8], [9] and fuel-cell power-conditioning systems [10].

The DAB in half bridge configuration shown in Figure 1, is composed of two inverters: the primary, formed by transistors Q_P and the secondary, composed by the transistors Q_S. The function of the two half-bridges is to impose a voltage difference on the inductance, L, generating a controlled current flow i_L. The inductance is responsible for accumulating energy in the form of current and then transferring it to the output capacitor C_o in the form of voltage. The transformer

The associate editor coordinating the review of this manuscript and approving it for publication was Kai Song.

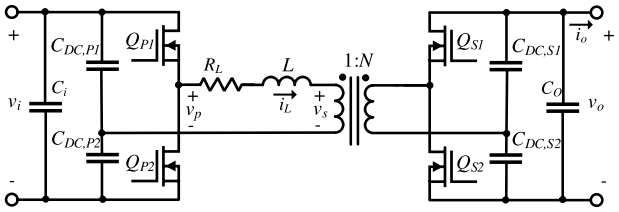

FIGURE 1. Dual active bridge converter.

serves as a linking element between primary and secondary half bridges allowing to establish the desired transformation ratio, N. The series capacitors C_{DC} are chosen to block the DC current levels and avoid saturation of the magnetic components. The main waveforms of the DAB are described in Figure 2. The voltage applied on the inductance L is the difference between the voltage of the primary inverter v_p and the voltage reflected by the transformer ratio N of the secondary inverter, v_s. The most common and widespread form of DAB control is based on phase shifting the voltage waveforms between primary and secondary. This phase shift ϕ makes possible to control the current flowing through the inductance: the greater the phase shift, the greater the

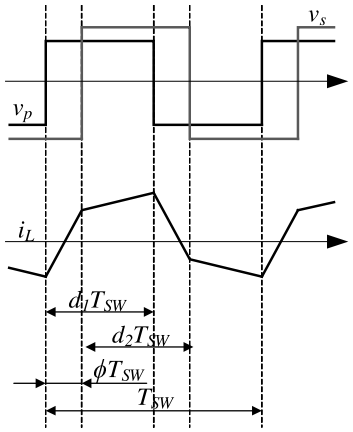

FIGURE 2. Dual active bridge waveforms.

current amplitude. As the operating point of the stage moves away from the optimum design point, mainly $v_o = Nv_i$, higher phase shifts are required. This also implies, as detailed in [11], a larger recirculating current through the inductance that is not converted into active power, significantly reducing efficiency. To mitigate that, the most used control is the triple phase shift control, summarized in [12], [13], which not only increases efficiency, but also raises the semiconductors soft switching range. This control require relatively high computational cost, careful implementation, detailed current handling to prevent the switches from losing soft switching and, because a third voltage level is needed, a full bridge on each side of the transformer. Moreover, in sectors like vehicle electrification and photovoltaic, given the aggressiveness of the market, the price of the converter is one of the most important factors. This leads to a search for cost reduction that ends up minimizing, whenever possible, the number of semiconductors and their drivers. For this reason, it is sometimes preferred to use a half bridge instead of a full bridge. In that case, advanced control methods cannot be implemented due to the lack of the additional control variable. In [14], the ϕ based control is compared with the variable switching frequency control, where it is shown that the latter has a better performance. Variable frequency control already appears in the literature, but the mathematical calculation of the transfer function that allows this control has not yet been proposed. This paper proposes an easy to implement, low computational cost and universal control method which is also capable of being implemented with half bridges, while maintaining high efficiency. As the main control, a fast inner loop that varies the switching frequency is in charge of regulating the output voltage. The Generalized State Space Average Model (GSSAM) for the DAB is fully developed, allowing to obtain the transfer function between the frequency and the output voltage. Then, to demonstrate the effectiveness and functionality of the proposed loop, a digital control design is suggested, simulated and validated experimentally. The generalized state model for the DAB has already been developed with several assumptions in a phase shift control [15]. In contrast to previous phase shift control applications, two additional state variables and an additional signal that is specific to the half-bridge structure has been included. This complicates the system and leads to the realization of the GSSAM from scratch. As a secondary control, the phase shift is varied slowly in order to improve the performance of the stage. This control, by means of perturbation and observation, operates to reduce the effective current at the input of the stage while maintaining the power delivered at the output and the zero voltage switching (ZVS) condition, tracking the maximum efficiency point. After the Introduction section, the main contribution of the work is fully developed in section II, where the GSSAM average model and the small-signal model from the switching frequency to the output voltage are fully explained for the DAB in half bridge configuration. Then, in Section III, a controller based on previous small-signal model is developed and experimentally validated with a prototype of 1 kW. An additional maximum efficiency point tracking control loop, based on phase shift control, is also presented and validated in Section IV, thus showing another important contribution of this paper. Finally, in the Section V, the conclusions of this work are exposed.

II. GENERALIZED STATE-SPACE AND SMALL-SIGNAL MODELING OF AN DUAL ACTIVE BRIDGE

The most commonly used method for modeling PWM converters is based on the averaged state space [16]. The application of the averaged state space model is used in converters such as the boost or buck converter where the state variables, voltages and currents, have high DC levels and higher order harmonics are neglected. In the case of the dual active bridge, this situation does not occur. The current flowing through the inductance does not contain DC level, only AC current. The model presented in this paper is based in the generalized state space model, explained in [17] and [18], where higher order harmonics are considered. In this paper, another control variable f_{sw}, high order harmonics of the output voltage and half-bridge adaptation signal are also taken into account. This allows the obtained small-signal model to be used in more regulators than the common phase shift control and if desired, for half-bridge configurations.

A. MATHEMATICAL FUNDAMENTALS OF THE GSSAM

In this section, the mathematical basis of the generalized state space average model is explained in depth to facilitate the understanding of the model. Fourier series allow any periodic and continuous signal in time, $f(t)$ to be decomposed into an infinite sum of sinusoidal or cosine functions called harmonics, n:

$$f(t) = \frac{a_0}{2} + \sum_{n=1}^{\infty}(a_n \cos(\frac{2\pi n}{T_{sw}}t)) + b_n \sin(\frac{2\pi n}{T_{sw}}t)) \quad (1)$$

where the period T_{sw} is the inverse of the switching frequency f_{sw}. The coefficient of the Fourier series a_0 refers to the 0 harmonic, $n = 0$, or DC level of the signal:

$$a_0 = \frac{2}{T_{sw}}\int_0^{T_{sw}} f(t)\mathrm{d}t \quad (2)$$

The remaining coefficients, a_n and b_n, represent the frequency content of the signal:

$$a_n = \frac{2}{T_{sw}} \int_0^{T_{sw}} f(t) \cos(\frac{2\pi n}{T_{sw}} t) \mathrm{d}t \tag{3}$$

$$b_n = \frac{2}{T_{sw}} \int_0^{T_{sw}} f(t) \sin(\frac{2\pi n}{T_{sw}} t) \mathrm{d}t \tag{4}$$

According to Euler's formulas:

$$\cos(nt) = \frac{e^{jnt} + e^{-jnt}}{2} \tag{5}$$

$$\sin(nt) = -j\frac{e^{jnt} - e^{-jnt}}{2} \tag{6}$$

Then, it is possible to rewrite (1) as:

$$f(t) = c_0 + \sum_{n=1}^{\infty} (c_n e^{jnt} + c_{-n} e^{-jnt}) = \sum_{n=-\infty}^{\infty} c_n e^{jnt} \tag{7}$$

where c_n can be calculated as:

$$c_n = \frac{1}{T_{sw}} \int_0^{T_{sw}} f(t) e^{-jn\omega_{sw} nt} \mathrm{d}t = \langle f \rangle_n \tag{8}$$

or separating the real and imaginary part:

$$c_n = \frac{1}{T_{sw}} \int_0^{T_{sw}} (\Re(c_n) - j\Im(c_n)) \mathrm{d}t = \langle f \rangle_n \tag{9}$$

being:

$$\Re(c_n) = \frac{1}{T_{sw}} \int_0^{T_{sw}} f(t) cos(\frac{2\pi n}{T_{sw}} t) = \langle f \rangle_n^{\Re} \tag{10}$$

and

$$\Im(c_n) = \frac{1}{T_{sw}} \int_0^{T_{sw}} f(t) sin(\frac{2\pi n}{T_{sw}} t) = \langle f \rangle_n^{\Im} \tag{11}$$

The time derivative of the coefficient $\langle f \rangle_n$ is obtained by applying Leibniz's law:

$$\begin{aligned} \frac{\mathrm{d}\langle f \rangle_n}{\mathrm{d}t} &= \frac{1}{T_{sw}} \int_0^{T_{sw}} \frac{\partial}{\partial t} (f(t) e^{jn\omega_{sw} t}) \mathrm{d}t \\ &= \frac{1}{T_{sw}} \int_0^{T_{sw}} \left(\frac{d}{dt} f(t) \right) e^{-jn\omega_{sw} t} \\ &\quad -jn\omega_{sw} f(t) e^{-jn\omega_{sw} t} \mathrm{d}t \end{aligned} \tag{12}$$

Substituting equation (8) into (12), it is finally reached:

$$\frac{\mathrm{d}\langle f \rangle_n}{\mathrm{d}t} = \langle \frac{\mathrm{d}f}{\mathrm{d}t} \rangle_n - jn\omega_{sw} \langle f \rangle_n \tag{13}$$

Let there be two Fourier coefficients, $\langle f \rangle_n$ and $\langle h \rangle_n$, the product of these is realized by discrete convolution:

$$\langle f \rangle_n * \langle h \rangle_n = \sum_{i=-\infty}^{\infty} \langle f \rangle_i \langle h \rangle_{n-i} \tag{14}$$

Solving (14) for the continuous level, $n = 0$, and the first-order terms, $n = \pm 1$, which are part of the first harmonic, it is obtained:

$$\langle f \rangle_0 * \langle h \rangle_0 = \langle f \rangle_{-1} \langle h \rangle_1 + \langle f \rangle_0 \langle h \rangle_0 + \langle f \rangle_1 \langle h \rangle_{-1} \tag{15a}$$

$$\langle f \rangle_{-1} * \langle h \rangle_{-1} = \langle f \rangle_{-1} \langle h \rangle_0 + \langle f \rangle_0 \langle h \rangle_{-1} \tag{15b}$$

$$\langle f \rangle_1 * \langle h \rangle_1 = \langle f \rangle_0 \langle h \rangle_1 + \langle f \rangle_1 \langle h \rangle_0 \tag{15c}$$

Assuming $\langle f \rangle_n$ must be a complex number, it is satisfied that its complementary is:

$$\langle f \rangle_n = \langle f \rangle_{-n}^* \tag{16}$$

Substituting (16) into (15), it is obtained:

$$\langle f \rangle_0 * \langle h \rangle_0 = \langle f \rangle_0 \langle h \rangle_0 + 2\langle f \rangle_1^{\Re} \langle h \rangle_1^{\Re} + 2\langle f \rangle_1^{\Im} \langle h \rangle_1^{\Im} \tag{17a}$$

$$\langle f \rangle_1^{\Im} * \langle h \rangle_1^{\Im} = \langle f \rangle_1^{\Im} \langle h \rangle_0 + \langle f \rangle_0 \langle h \rangle_1^{\Im} \tag{17b}$$

$$\langle f \rangle_1^{\Re} * \langle h \rangle_1^{\Re} = \langle f \rangle_0 \langle h \rangle_1^{\Re} + \langle f \rangle_1^{\Re} \langle h \rangle_0 \tag{17c}$$

B. APPLICATION OF THE METHOD TO THE DAB

The equations developed in Subsection II-A are applied to the dual active bridge shown in Figure 1. The square voltage waveforms of the primary v_p and secondary v_s half bridges are proportional to the signals $u_1(t)$ and $u_2(t)$, being:

$$u_1(t) = \begin{cases} 1 & 0 < t \leq d_1 T_{sw} \\ -1 & d_1 T_{sw} < t \leq T_{sw} \end{cases} \tag{18}$$

and

$$u_2(t) = \begin{cases} 1 & \phi T_{sw} < t \leq (\phi + d_2) T_{sw} \\ -1 & (\phi + d_2) T_{sw} < t \leq T_{sw}(1 + \phi) \end{cases} \tag{19}$$

On the other hand, in the half bridge, the energy is transferred from the inductance L to the capacitor C when the signal $u_2(t)$ is positive, giving place to $u_3(t)$:

$$u_3(t) = \begin{cases} 1 & \phi T_{sw} < t \leq (\phi + d_2) T_{sw} \\ 0 & (\phi + d_2) T_{sw} < t \leq T_{sw}(1 + \phi) \end{cases} \tag{20}$$

Choosing as state variables the current in the inductance L, $\langle i_L(t) \rangle$ and the voltage on the output capacitor C_o, $\langle v_o(t) \rangle$, the differential equations of the stage shown in Figure 1 result in:

$$\frac{\mathrm{d}i_L(t)}{\mathrm{d}t} = -\frac{R_L}{L} i_L(t) + \frac{u_1(t)}{2L} v_i(t) - \frac{u_2(t)}{2NL} v_o(t) \tag{21}$$

$$\frac{\mathrm{d}v_o(t)}{\mathrm{d}t} = -\frac{1}{RC_o} v_o(t) + \frac{u_3(t)}{C_o N} i_L(t) \tag{22}$$

It is important to remark that the current i_L does not contain a continuous level, so it is necessary to calculate at least the first harmonic $n = 1$ to obtain a valid model. Applying (17) in (21) and (22), gives the corresponding Fourier coefficients:

$$\frac{\mathrm{d}\langle i_L \rangle_n}{\mathrm{d}t} = -\frac{R_L}{L} \langle i_L \rangle_n + \frac{\langle u_1 \rangle_n * \langle v_i \rangle_n}{2L} - \frac{\langle u_2 \rangle_n * \langle v_o \rangle_n}{2NL} \tag{23}$$

$$\frac{\mathrm{d}\langle v_o \rangle_n}{\mathrm{d}t} = -\frac{1}{RC_o} \langle v_o \rangle_n + \frac{\langle u_3 \rangle_n * \langle i_L \rangle_n}{NC_o} \tag{24}$$

Representing (23) and (24) up to the first harmonic ($n = 0$,-1,1) and applying (17) results in:

$$\begin{aligned} \frac{\langle \mathrm{d}i_L \rangle_1^{\Re}}{\mathrm{d}t} &= -\frac{R_L}{L} \langle i_L \rangle_1^{\Re} + \frac{\langle u_1 \rangle_0 \langle v_i \rangle_1^{\Re} + \langle u_1 \rangle_1^{\Re} \langle v_i \rangle_0}{2L} \\ &\quad - \frac{\langle u_2 \rangle_0 \langle v_o \rangle_1^{\Re} + \langle u_2 \rangle_1^{\Re} \langle v_o \rangle_0}{2NL} + \omega_{sw} \langle i_L \rangle_1^{\Im} \end{aligned} \tag{25}$$

$$\frac{\langle \mathrm{d}i_L\rangle_1^{\Im}}{\mathrm{d}t} = -\frac{R_L}{L}\langle i_L\rangle_1^{\Im} + \frac{\langle u_1\rangle_0\langle v_i\rangle_1^{\Im} + \langle u_1\rangle_1^{\Im}\langle v_i\rangle_0}{2L} - \frac{\langle u_2\rangle_0\langle v_o\rangle_1^{\Im} + \langle u_2\rangle_1^{\Im}\langle v_o\rangle_0}{2NL} - \omega_{sw}\langle i_L\rangle_1^{\Re} \quad (26)$$

$$\frac{\langle \mathrm{d}v_0\rangle_0}{\mathrm{d}t} = -\frac{\langle v_o\rangle_0}{RC_o} + \frac{2(\langle u_3\rangle_1^{\Re}\langle i_L\rangle_1^{\Re} + \langle u_3\rangle_1^{\Im}\langle i_L\rangle_1^{\Im})}{NC_o} \quad (27)$$

$$\frac{\langle \mathrm{d}v_0\rangle_1^{\Re}}{\mathrm{d}t} = -\frac{\langle v_o\rangle_1^{\Re}}{RC_o} + \frac{\langle u_3\rangle_0^{\Re}\langle i_L\rangle_1^{\Re}}{NC_o} + \omega_{sw}\langle v_o\rangle_1^{\Im} \quad (28)$$

$$\frac{\langle \mathrm{d}v_0\rangle_1^{\Im}}{\mathrm{d}t} = -\frac{\langle v_o\rangle_1^{\Im}}{RC_o} + \frac{\langle u_3\rangle_0^{\Im}\langle i_L\rangle_1^{\Im}}{NC_o} - \omega_{sw}\langle v_o\rangle_1^{\Re} \quad (29)$$

where $w_{sw} = 2\pi f_{sw}$.

Considering that $v_i(t)$ is constant, it is satisfied

$$\langle v_i\rangle_1^{\Re} = \langle v_i\rangle_1^{\Im} = 0 \quad (30)$$

so these state variables can be eliminated.

Defining the state vector $\boldsymbol{x}$ as:

$$\boldsymbol{x} = [\langle i_L\rangle_1^{\Re}\ \langle i_L\rangle_1^{\Im}\ \langle v_o\rangle_0\ \langle v_o\rangle_1^{\Re}\ \langle v_o\rangle_1^{\Im}]' \quad (31)$$

and the input vector $\boldsymbol{u}$:

$$\boldsymbol{u} = [\langle v_i\rangle_0] \quad (32)$$

equations (25)-(29) can be represented in matrix form, obtaining the state space model:

$$\dot{\boldsymbol{x}} = \boldsymbol{A}\boldsymbol{x} + \boldsymbol{B}\boldsymbol{u} \quad (33)$$

Being $\boldsymbol{A}$:

$$\boldsymbol{A} = \begin{bmatrix} -\frac{R_L}{L} & \omega_{sw} & -\frac{\langle u_2\rangle_1^{\Re}}{2NL} & -\frac{\langle u_2\rangle_0}{2NL} & 0 \\ -\omega_{sw} & -\frac{R_L}{L} & -\frac{\langle u_2\rangle_1^{\Im}}{2NL} & 0 & -\frac{\langle u_2\rangle_0}{2Ln} \\ \frac{2\langle u_3\rangle_1^{\Re}}{NC_o} & \frac{2\langle u_3\rangle_1^{\Im}}{NC_o} & -\frac{1}{C_oR} & 0 & 0 \\ \frac{\langle u_3\rangle_0}{NC_o} & 0 & 0 & -\frac{1}{C_oR} & \omega_{sw} \\ 0 & \frac{\langle u_3\rangle_0}{NC_o} & 0 & -\omega_{sw} & -\frac{1}{C_oR} \end{bmatrix} \quad (34)$$

and $\boldsymbol{B}$:

$$\boldsymbol{B} = \begin{bmatrix} \frac{\langle u_1\rangle_1^{\Re}}{2L} \\ \frac{\langle u_1\rangle_1^{\Im}}{2L} \\ 0 \\ 0 \\ 0 \end{bmatrix} \quad (35)$$

The continuous and first-order Fourier coefficients of the signals $u_1(t)$, $u_2(t)$ and $u_3(t)$ are obtained from developing the Fourier series of the signals (18), (19) and (20) by means of (1) and (9). In this way, it is obtained for $u_1(t)$:

$$\langle u_1\rangle_0 = 2d_1 - 1 \quad (36a)$$

$$\langle u_1\rangle_1^{\Re} = \frac{\sin(2\pi d_1)}{\pi} \quad (36b)$$

$$\langle u_1\rangle_1^{\Im} = \frac{\cos(2\pi d_1) - 1}{\pi} \quad (36c)$$

for $u_2(t)$:

$$\langle u_2\rangle_0 = 2d_2 - 1 \quad (37a)$$

$$\langle u_2\rangle_1^{\Re} = \frac{\sin(2\pi\phi + 2\pi d_2) - \sin(2\pi\phi)}{\pi} \quad (37b)$$

$$\langle u_2\rangle_1^{\Im} = \frac{\cos(2\pi\phi + 2\pi d_2) - \cos(2\pi\phi)}{\pi} \quad (37c)$$

and for $u_3(t)$

$$\langle u_3\rangle_0 = d_2 \quad (38a)$$

$$\langle u_3\rangle_1^{\Re} = \frac{\sin(2\pi\phi + 2\pi d_2) - \sin(2\pi\phi)}{\pi} \quad (38b)$$

$$\langle u_3\rangle_1^{\Im} = \frac{\cos(2\pi\phi + 2\pi d_2) - \cos(2\pi\phi)}{\pi}. \quad (38c)$$

C. SMALL SIGNAL MODEL

The system represented in (33) contains non-linear terms. For this reason, to design the control loop, it is necessary to linearize the system around an equilibrium point $\boldsymbol{x_{eq}}$, where there are no significant variations.

The equilibrium point $\boldsymbol{x_{eq}}$ is obtained from eliminating the disturbances in (33), $\dot{\boldsymbol{x}} = 0$, and solving:

$$\boldsymbol{x_{eq}} = -\boldsymbol{A}^{-1}\boldsymbol{B}\boldsymbol{u} \quad (39)$$

By introducing a small perturbation in the control variables, in this case: $\hat{\phi}$, $\hat{d}_1$, $\hat{d}_2$ or $\hat{\omega}_{sw}$, the state variables will vary with respect to the equilibrium point. Perturbing the system around the equilibrium point yields the small-signal model. Linear approximation of the system is obtained through the first order term of the Taylor Series representation: Let $f(x)$ be continuous and differentiable, x_{eq} the equilibrium point and $\hat{x}$ a small perturbation, it is satisfied:

$$\hat{x} = x - x_{eq} \quad (40)$$

and

$$f(x) = \hat{\dot{x}} \approx f(x_{eq}) + f'(x_{eq})(x - x_{eq}) = 0 + f'(x_{eq})\hat{x} \quad (41)$$

The first order derivative $f'(x_{eq})$ at the equilibrium point is calculated by the Jacobian of the system. Being:

$$f(\boldsymbol{x}, \phi, d_1, d_2, \omega_{sw}) = (\boldsymbol{A}\boldsymbol{x} + \boldsymbol{B}\boldsymbol{u}) \quad (42)$$

Applying the Jacobian matrix in (42)

$$\frac{\mathrm{d}\langle\hat{\boldsymbol{x}}\rangle}{\mathrm{d}t} = \nabla f(\boldsymbol{x}, \phi, d_1, d_2, \omega_{sw}) \quad (43)$$

it is obtained the small-signal representation of the system:

$$\hat{\dot{x}} = \hat{\boldsymbol{A}}\hat{x} + \hat{\boldsymbol{B}}\hat{u} + \hat{\boldsymbol{E}}_1\hat{\phi} + \hat{\boldsymbol{E}}_2\hat{d}_1 + \hat{\boldsymbol{E}}_3\hat{d}_2 + \hat{\boldsymbol{E}}\hat{\omega}_{sw} \quad (44)$$

where:

$$\hat{\boldsymbol{A}} = \begin{bmatrix} -\frac{R_L}{L} & \omega_{sw} & -\frac{\langle U_2\rangle_1^{\Re}}{2NL} & -\frac{\langle U_2\rangle_0}{2NL} & 0 \\ -\omega_{sw} & -\frac{R_L}{L} & -\frac{\langle U_2\rangle_1^{\Im}}{2NL} & 0 & -\frac{\langle U_2\rangle_0}{2Ln} \\ \frac{2N\langle U_3\rangle_1^{\Re}}{C_o} & \frac{2N\langle U_3\rangle_1^{\Im}}{C_o} & -\frac{1}{CR} & 0 & 0 \\ \frac{N\langle U_3\rangle_0}{C_o} & 0 & 0 & -\frac{1}{C_oR} & \omega_{sw} \\ 0 & \frac{N\langle U_3\rangle_0}{C_o} & 0 & -\omega_{sw} & -\frac{1}{C_oR} \end{bmatrix} \quad (45)$$

$$\hat{\boldsymbol{x}} = [\langle\hat{i}_L\rangle_1^{\Re}\ \langle\hat{i}_L\rangle_1^{\Im}\ \langle\hat{v}_o\rangle_0\ \langle\hat{v}_o\rangle_1^{\Re}\ \langle\hat{v}_o\rangle_1^{\Im}]' \quad (46)$$

$$\hat{\boldsymbol{B}} = \begin{bmatrix} \frac{\langle U_1 \rangle_1^{\Re}}{L} \\ \frac{\langle U_1 \rangle_1^{\Im}}{L} \\ 0 \\ 0 \\ 0 \end{bmatrix} \tag{47}$$

$$\hat{\boldsymbol{E}} = \begin{bmatrix} \langle I_L \rangle_1^{\Im} \\ -\langle I_L \rangle_1^{\Re} \\ 0 \\ \langle V_o \rangle_1^{\Im} \\ -\langle V_o \rangle_1^{\Re} \end{bmatrix} \tag{48}$$

Capitalized letters in the above equations represent the variables at their equilibrium point.

D. TRANSFER FUNCTION BETWEEN OUTPUT VOLTAGE AND SWITCHING FREQUENCY

The state variable to be usually regulated in this topology is the DC output voltage v_o. In this work, v_o is controlled by f_{sw}. Therefore, using (44), (45), (46) and (48) the small-signal representation required to design the controller become:

$$\frac{\mathrm{d}\hat{\boldsymbol{x}}}{\mathrm{d}t} = \hat{\boldsymbol{A}}\hat{\boldsymbol{x}} + \hat{\boldsymbol{E}}\hat{\omega}_{sw} \tag{49}$$

The control signal to output voltage transfer function is denoted as:

$$G_{v\omega_{sw}}(s) = \boldsymbol{C}(s\boldsymbol{I} - \hat{\boldsymbol{A}})\hat{\boldsymbol{E}} \tag{50}$$

where $\boldsymbol{C}$ is:

$$\boldsymbol{C} = [0\ 0\ 1\ 0\ 0] \tag{51}$$

Substituting the parameters of TABLE 1 in (50), the following transfer function is obtained:

$$G_{vf_{sw}}(s) = \frac{72015(s - 8.069 \times 10^5)}{(s + 166.5)(s^2 + 5.136s + 8.171 \times 10^{10})} \tag{52}$$

It is important to remark that, due the calculation of the First Fourier harmonic for obtaining the DAB model, equation (52) presents high-frequency modeling effects in form of resonance and non minimum phase dynamics. The high frequency resonance is placed at the switching frequency and the right half plane zero represents the delay in power output transmission, which is related to $d_2 T_{sw}$ plus ϕ. However, these high frequency effects are far away of the useful frequency range of a small-signal model, which is below a half of the switching frequency, and usually are not taken into account for control purposes. The obtained transfer function is represented in the Bode diagram of FIGURE 3. In this Figure, it is also possible to observe a perfect agreement between the frequency representation of the obtained analytical model and the obtained by simulation using Matlab/Simulink.

III. DIGITAL CONTROLLER DESIGN AND EXPERIMENTAL VERIFICATION

This section develops as an example a digital control based on the transfer function obtained in the previous section to demonstrate its benefits and feasibility.

TABLE 1. DAB Equilibrium point parameters.

Parameter	Value
v_{in}	200 V
v_o	200 V
ϕ	0.1
d_1	0.5
d_2	0.5
f_{sw}	45 kHz
N	1
L	20 μH
R_L	240 mΩ
C_o	150 μF
R_{load}	40 Ω

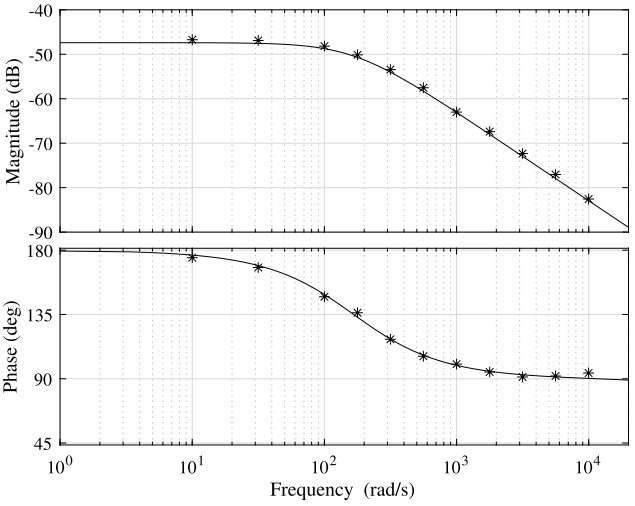

FIGURE 3. Frequency response of $G_{vf_{sw}}(s)$. Solid line: Analytical model results. Asterisks: Simulation.

A. CONTROLLER DESIGN

A design based on emulation is proposed, where a continuous controller is initially designed and then discretized. Since the controller is discrete, a delay t_d occurs between the sampling instant and the update of the control action. This delay is represented by the transfer function:

$$G_{del}(s) = e^{-t_d s} \tag{53}$$

So, the new continuous plant with the included delay results in:

$$G_{vf_{sw},del}(s) = G_{vf_{sw}}(s)G_{del}(s) \tag{54}$$

A PI controller to ensure output voltage regulation and zero steady-state error is proposed as follows:

$$Gc(s) = \frac{-1}{|G_{vf_{sw},del}(j\omega_o)|}\left(\frac{s + \omega_I}{s}\right) \tag{55}$$

A simple design process of this PI is done choosing the crossover frequency ω_o regarding the desired Phase Margin, setting ω_I one decade below ω_o and adding the gain needed to ensure loop gain 0 dB crossing at ω_o. This is done dividing by $|G_{vf_{sw},del}(j\omega_o)|$ that represents the magnitude gain of (54)

at ω_o. Once the $G_c(s)$ is obtained, it can be discretized using the bilinear transform which maps the left half of the complex s-plane to the unit circle in the z-plane:

$$Gc(z) = Gc(s)|_{s=\frac{2}{T_s}\frac{z-1}{z+1}} \tag{56}$$

where T_s is the sampling period.

B. SIMULATION AND EXPERIMENTAL RESULTS

In order to show the model utility, a digital PI controller is designed following the procedure described in Section III-A. A loop gain crossover frequency of 1000 rad/s its sufficiently below of the minimum switching frequency and gives a conservative Phase Margin value around 90°. As explained in Section III-A, the zero of the PI is placed one decade below the crossover frequency, i.e. $\omega_I = 100$ rad/s. The gain of the controller is adjusted to achieve 0 dB loop gain crossing at $\omega_o = 1000$ rad/s, thus giving $1/|G_{vf_{sw},del}(j\omega_o)| = 63$ dB, as can be seen in FIGURE 4.

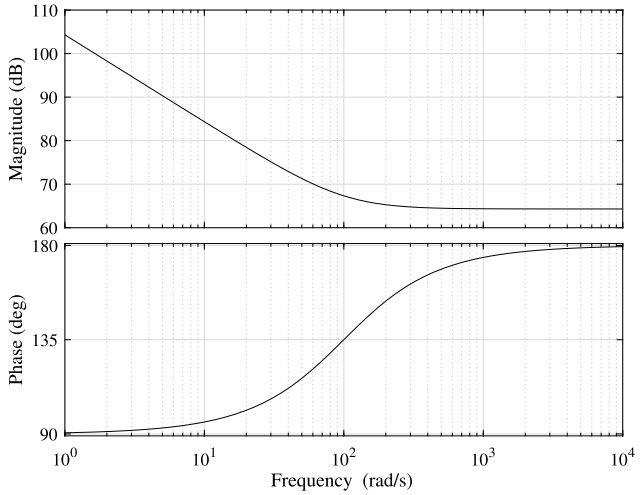

FIGURE 4. Frequency response of $G_c(s)$.

The open loop gain, $G_{ol}(s)$ of the system, defined as

$$G_{ol}(s) = G_c(s)G_{v,f_{sw}}(s)G_{del}(s) \tag{57}$$

is represented in FIGURE 5 using the parameters of TABLE 2. From FIGURE 5, it can be seen than the phase margin is around 90° ensuring the stability of the system.

TABLE 2. Controller parameters.

Parameter	Value
ω_c	1000
ω_I	100
t_d	33.33μs
T_s	6.67μs

The continuous controller is discretized using the Bilinear transformation with a sample time T_s, that ensures that all the poles are located inside the unit circle of the z-plane.

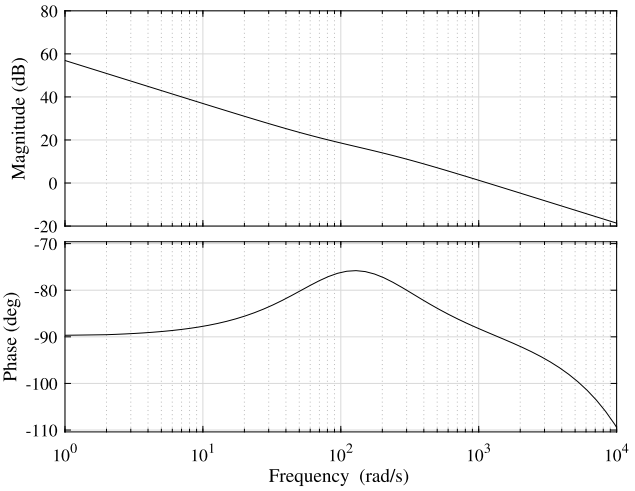

FIGURE 5. Frequency response of converter gain loop.

The discretized controller, $G_c(z)$ is implemented in the prototype shown in FIGURE 6, which is based on TABLE 1. Selected semiconductors are STW70N60DM2 and the magnetic components are made of ferrite N87. The control is implemented in a FPGA from the Artix-7 family.

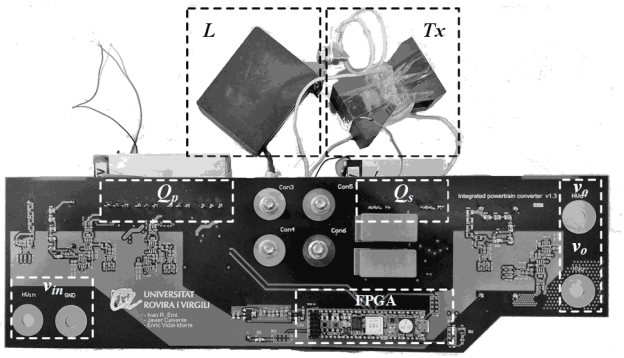

FIGURE 6. Converter prototype.

FIGURE 7 compares the response obtained by simulation with the experimental response to a 25% increase in the reference output voltage. Experimental and simulation transient behaviors agree and show that the system its able to reach the new set point with zero stationary error. Experimental and simulated time responses for 25% of load perturbation are presented respectively in FIGURE 8. Both experimental and simulation transient behavior agree again, showing the system is able to recover again its zero output voltage error stationary state, validating the theoretical predictions and the feasibility of the controller. Similarly, FIGURE 9 shows how the regulator presented in the previous subsection is able to maintain the output voltage in the presence of a 25 % variation in the converter input voltage.

IV. MAXIMUM EFFICIENCY POINT TRACKING

As it has been seen, when varying the switching frequency using the controller designed in previous section, it is possible

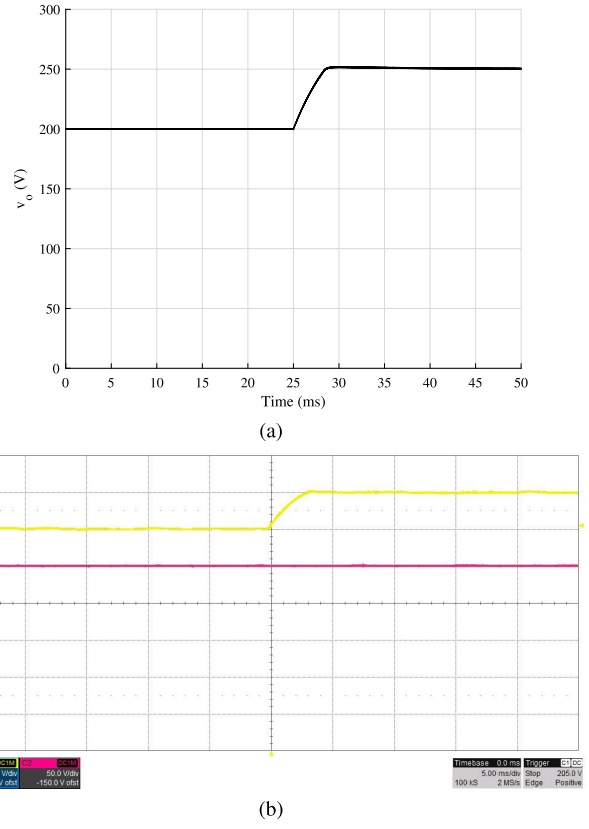

FIGURE 7. Voltage reference variation. (a) Simulated. (b)Experimental. From top to bottom: Output voltage v_o (50 V/div) and input voltage v_i (50 V/div). Timescale (5 ms/div).

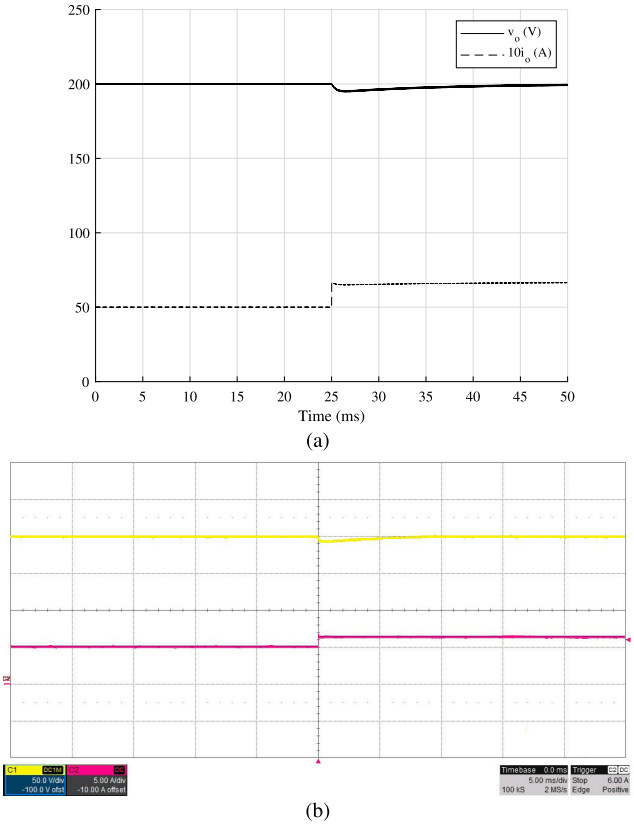

FIGURE 8. Output voltage response to load perturbation of 25%. (a) Simulated- (b) Experimental. From top to bottom: Output voltage v_o (50 V/div) and output current i_o (5 A/div). Timescale (5 ms/div).

to regulate the output variable relatively quickly in front of load disturbances and reference changes. This leaves free the control variable most commonly used in this topology, the phase shift ϕ. This variable could be left fixed at a value that guarantees the full range of operation, but taking advantage of this additional degree of freedom, the aim is to improve the efficiency of the converter.

A. CONVERTER LOSSES AND CONTROL MOTIVATION

Previous works [19], [20] describe how the conduction loss is dominant in the total power loss, which implies that the overall system efficiency can be improved reducing the RMS value of $i_L(t)$ or the input current $i_{in}(t)$. Thus, the minimization of $I_{in,rms}$ can be adopted as the optimization objective. Consequently, the reactive input current is reduced. It is important to note, that switching looses are less dominant since ZVS exists during turn on, while at turn off, they are compensated by a lower switching current. According to FIGURE 2, during one switching cycle T_{sw}, four current slopes can be distinguished in the inductor L depending on the voltage difference between v_p and v_s:

$$m_{i_L}(\tau) = \begin{cases} m_{i_L,1} & 0 < \tau \leq \phi T_{sw} \\ m_{i_L,2} & \phi T_{sw} < \tau \leq d_1 T_{sw} \\ m_{i_L,3} & d_1 T_{sw} < \tau \leq (d_2 + \phi) T_{sw} \\ m_{i_L,4} & (d_2 + \phi) T_{sw} < \tau \leq T_{sw} \end{cases} \tag{58}$$

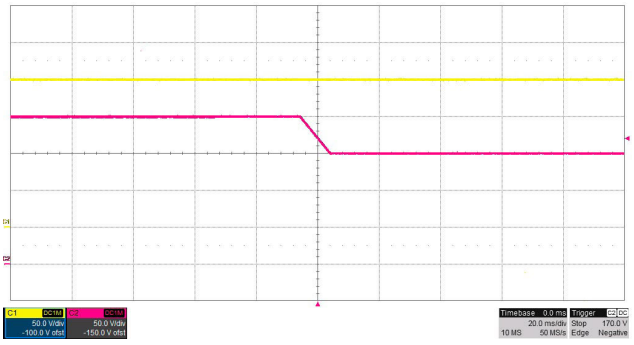

FIGURE 9. Output voltage response to input voltage perturbation of 25%. From top to bottom: Output voltage v_o (50 V/div) and input voltage v_i (50 V/div). Timescale (20 ms/div).

where $\tau = t - nT_{sw}$.

$$m_{iL,1} = \frac{d_2 v_o + (1 - d_1) N v_i}{LN} \tag{59}$$

$$m_{iL,2} = \frac{(d_2 - 1) v_o + (1 - 1d_1) N v_i}{LN} \tag{60}$$

$$m_{iL,3} = \frac{-(1 - d_2) v_o / N - d_1 v_i}{L} \tag{61}$$

$$m_{iL,4} = \frac{d_2 v_o / N - d_1 v_i}{L} \tag{62}$$

Once inductor current slope is obtained, instant inductor current $i_L(t)$ can be determined as the initial current $i_L(nT_{sw})$

plus the increment $\Delta i_L(\tau)$:

$$i_L(t) = i_L(nT_{sw}) + \Delta i_L(\tau) \tag{63}$$

$$\Delta i_L(\tau) = \begin{cases} \Delta i_{L,1}(\tau) & 0 < \tau \leq \phi T_{sw} \\ \Delta i_{L,2}(\tau) & \phi T_{sw} < \tau \leq d_1 T_{sw} \\ \Delta i_{L,3}(\tau) & d_1 T_{sw} < \tau \leq (d_2+\phi) T_{sw} \\ \Delta i_{L,4}(\tau) & (d_2+\phi) T_{sw} < \tau \leq T_{sw} \end{cases} \tag{64}$$

where

$$\Delta i_{L,1}(\tau) = m_{iL,1}\tau \tag{65}$$

$$\Delta i_{L,2}(\tau) = m_{iL,1}\phi T_{sw} + m_{iL,2}(\tau - \phi T_{sw}) \tag{66}$$

$$\Delta i_{L,3}(\tau) = m_{iL,1}\phi T_{sw} + m_{iL,2}(d_1 - \phi)T_{sw} + m_{iL,3}(\tau - d_1 T_{sw}) \tag{67}$$

$$\Delta i_{L,4}(\tau) = m_{iL,1}\phi T_{sw} + m_{iL,2}(d_1 - \phi)T_{sw} + m_{iL,3}(d_2 + \phi - d_1)T_{sw} + m_{iL,4}(\tau - (\phi + d_2)T_{sw}) \tag{68}$$

Since series capacitor exists, average current must be zero. It is assumed that the time constant imposed by the series capacitors $C_{DC,x}$ is small and do not affect the system. That means, the value that makes the average current equal to zero corresponds to $i_L(nT_{sw})$ during each switching period:

$$i_L(nT_{sw}) + \frac{1}{T_{sw}}\int_0^{T_{sw}} \Delta i_L(\tau)\mathrm{d}\tau = 0 = i_L(nT_{sw}) + \frac{1}{T_{sw}}\left(\int_0^{\phi T_{sw}} \Delta i_{L,1}(\tau)\mathrm{d}\tau + \int_{\phi T_{sw}}^{d_1 T_{sw}} \Delta i_{L,2}(\tau)\mathrm{d}\tau + \int_{d_1 T_{sw}}^{(d_2+\phi)T_{sw}} \Delta i_{L,3}(\tau)\mathrm{d}\tau + \int_{(d_2+\phi)T_{sw}}^{T_{sw}} \Delta i_{L,4}(\tau)\mathrm{d}\tau\right) \tag{69}$$

The input effective current can be calculated as:

$$I_{in,rms} = \left(\frac{1}{T_{sw}}\int_{d1T_{sw}}^{T_{sw}} i_L(\tau)^2\,\mathrm{d}\tau\right)^{1/2} \tag{70}$$

which by solving the equation and substituting d_1 and d_2 by 0.5, results in:

$$I_{in,rms} = \frac{\sqrt{{v_o}^2 + \left(-64\,n\,\phi^3 + 48\,N\,\phi^2 - 2\,n\right)\,v_b v_o + N^2\,{v_i}^2}}{8\sqrt{6}L\;|f_{sw}|\,|n|} \tag{71}$$

Input power P_i can be calculated as the current flowing through the inductor multiplied by the applied input voltage at the first inductor terminal:

$$\langle P_i\rangle_{T_{sw}} = \frac{1}{T_{sw}}\int_0^{T_{sw}} v_p(t) i_L(t)\,\mathrm{d}t = \frac{1}{T_{sw}}(E_1 + E_2 + E_3 + E_4) \tag{72}$$

where

$$E_1 = \int_0^{\phi T_{sw}} v_i(1-d_1) i_L(\tau))\,\mathrm{d}\tau \tag{73}$$

$$E_2 = \int_{\phi T_{sw}}^{d_1 T_{sw}} v_i(1-d_1) i_L(\tau)\,\mathrm{d}\tau \tag{74}$$

$$E_3 = \int_{d_1 T_{sw}}^{d_2+\phi T_{sw}} -v_i d_1 i_L(\tau)\,\mathrm{d}\tau \tag{75}$$

$$E_4 = \int_{d_2+\phi T_{sw}}^{T_{sw}} -v_i d_1 i_L(\tau)\,\mathrm{d}\tau \tag{76}$$

Assuming high efficiency, the output power P_o equals P_i and equating d_1 to d_2:

$$\langle P_o\rangle_{T_{sw}} = \frac{\left(-\phi^2 + \left(-2d^2 + 2d\right)\phi\right) v_i v_o}{L f_{sw} N} \tag{77}$$

By solving for the variable f_{sw} in the previous function and substituting in (71), $I_{in,rms}$ can be rewritten as:

$$I_{in,rms} = \frac{|P_o|\,\sqrt{{v_o}^2 + \left(-64\phi^3 + 48\phi^2 - 2\right)\,v_i v_o + {v_i}^2}}{2\sqrt{6}\,\left|2\phi^2 - \phi\right|\,v_i v_o} \tag{78}$$

Using the parameters of TABLE 1 in equation (78), FIGURE 10 is obtained. It can be seen that for the same P_o, the effective input-current can increased or reduced depending on v_o and ϕ. While v_o is tightly regulated to achieve the voltage reference setting, ϕ can be modified to reduce the effective input current. It is important to note that when $v_i = Nv_o$, the optimum ϕ value would be almost zero and switching frequency to maintain P_o results too low. This would imply the use of large volume magnetic components and the loss of ZVS. For this reason, a minimum switching frequency, $f_{sw,min}$ must always be considered, which is also translated into a minimum phase shift, preventing the magnets from saturating due to excess current and ensuring ZVS.

B. MAXIMUM EFFICIENCY POINT TRACKING STRATEGY CONTROL LOOP

As demonstrated in previous subsection, the efficiency of the topology can be improved reducing $I_{in,rms}$ by varying ϕ. Finding the optimal ϕ value would involve solving the derivative of ϕ and equating to 0 in equation (78), which results in an equation that is difficult to implement. A possible solution would be to use a look up table, but due to component tolerances, switching losses and variations caused by thermal effects, the actual instantaneous optimum point would not be reached. To simplify and ease the computational cost and hardware required to perform the measurement, taking into account the analysis of Section IV-A and the relationship:

$$I_{in} = \frac{P_o + I_{in,rms}^2 R_{loss}}{V_i} \tag{79}$$

where capital letters represent the average values and R_{loss} the overall loss resistor, the following method is proposed. The maximum efficiency point tracking (MEPT) intends to

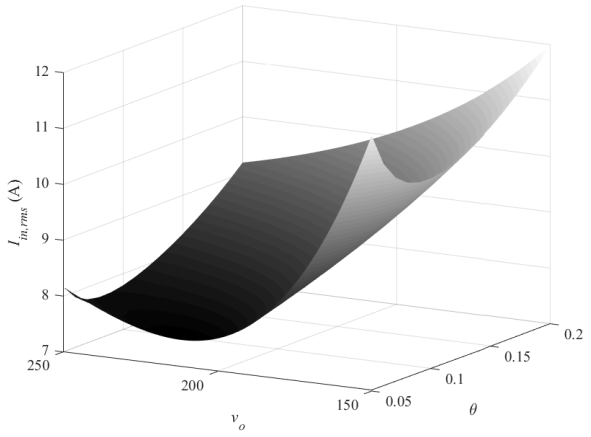

FIGURE 10. $I_{in,rms}$ variation depending on v_o and ϕ.

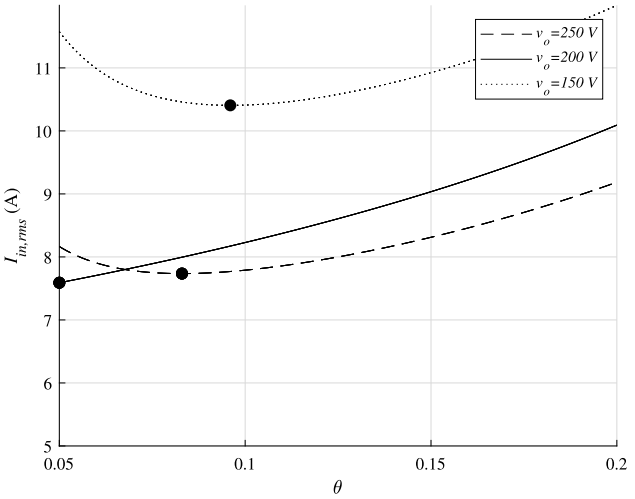

FIGURE 11. Detail of $I_{in,rms}$ variation.

establish a secondary control loop that slowly varies ϕ to find the optimum operating point of the converter by reducing the averaged current consumed at the input I_{in} and ensure ZVS while maintaining the power delivered at the output. In other words, modify ϕ to minimize equations (78) and (79). For this aim, it is proposed to use the Perturb and Observe method, a widely known technique that has proven its effectiveness in the solar energy sector and improved in [21], [22]. In this technique, a small perturbation is applied to provoke the input power variation. With a given period, the phase shift is modified and the evolution of the current at the input is observed. At the end of the cycle, if the filtered input current I_{in} is lower, ϕ is varied again in the same direction. Conversely, if I_{in} is higher than in the previous cycle, ϕ is varied in the opposite direction in this cycle. Consequently, the RMS current will evolve to the corresponding minimum current point, marked with a black point FIGURE 11. It is important to note that when there is a change in ϕ, f_{sw} varies to maintain regulation at the output. Therefore, the increase or decrease in the phase shift step should not be too high to maintain v_o without ripple. By solving for f_{sw} and linearizing (77), the variation of f_{sw} as a function of ϕ is obtained:

$$\hat{f}_{sw} = \frac{\left(D_1 - {D_1}^2 - \theta\right) V_b V_o}{L\, P_o N} \hat{\phi} \tag{80}$$

By making three cuts at different voltages in FIGURE 10, FIGURE 11 is obtained, where the existence of an optimum ϕ value for each voltage that reduces the effective current in the system can be seen in more detail. In addition, this control is in charge of maintaining the ZVS operation and ensure that the operation point is able to deliver the required output power, so ϕ should never be less than a certain value, ϕ_{min}. It is important to maintain the ZVS condition to prevent switching losses from increasing significantly. To guarantee ZVS in all semiconductors, the anti-parallel diode must conduct and discharge the MOSFET capacities before it turns on:

$$i(t = T_{sw}) < -I_{min} \tag{81a}$$

$$i(t = (\phi + d_2)T_{sw}) < -I_{min} \tag{81b}$$

$$i(t = d_1 T_{sw}) > I_{min} \tag{81c}$$

$$i(t = \phi T_{sw}) > I_{min} \tag{81d}$$

I_{min} represents the minimum required current to discharge the parallel capacitance of the switching devices. Detailed information about ZVS capacitances discharge can be found in [23]. Rewriting (81) and (77), it is obtained:

$$\phi_{min} > \begin{cases} -\dfrac{N v_{in} - v_o + 8 I_{min} L N f_{sw}}{4 v_o} \\ \dfrac{N v_{in} - v_o - 8 I_{min} L N f_{sw}}{4 N v_{in}} \\ -\dfrac{N v_{in} - v_o - 8 I_{min} L N f_{sw}}{4 v_o} \\ \dfrac{N v_{in} - v_o + 8 I_{min} L N f_{sw}}{4 N v_{in}} \\ \dfrac{\sqrt{v_i}\sqrt{v_o}\sqrt{v_i v_o - 32\, L\, P_o f_{sw,min} n} + v_i v_o}{4 v_i v_o} \end{cases} \tag{82}$$

where $f_{sw,min}$ is the minimum allowed switching frequency of the converter. The maximum value of ϕ from equation (82) must be selected as the low saturation limit, ϕ_{min}. The control steps described above are summarized in the flow diagram in FIGURE 12.

C. EXPERIMENTAL MEPT VALIDATION

FIGURE 13 shows how once the equilibrium point is reached, the phase control starts to act and reduces the input current by about 15%. Once the optimum point in FIGURE 13 has been reached, the converter waveforms can be seen in more detail in FIGURE14. In it, it can be observed that the stage operates in ZVS fulfilling equation (81). It is also important to note that the final phase shift match the expected value in FIGURE 11, since ϕ is at the minimum allowed value given by (82), 0.056 for $f_{sw,min} = 25$ kHz. Similarly occurs when $v_o = 250$ V as shown in FIGURE15. Equation (81) is also fulfilled, ensuring ZVS and ϕ results 0.85, matching

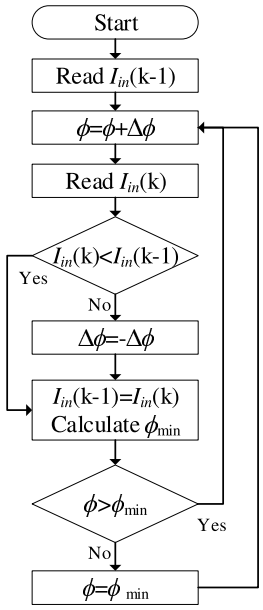

FIGURE 12. Maximum efficiency point tracking control flowchart.

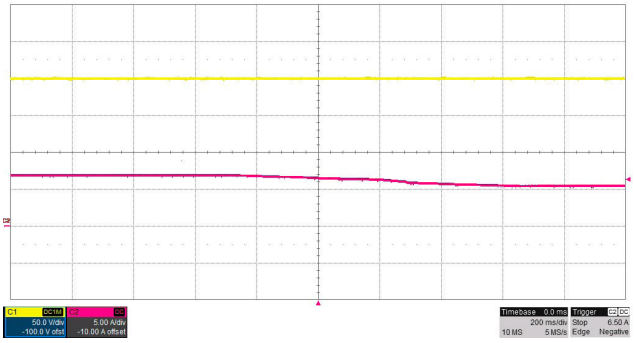

FIGURE 13. Effect of maximum efficiency point tracking control on i_i.From top to bottom: Output voltage v_o (50 V/div) and input current i_i (5 A/div). Timescale (200 ms/div).

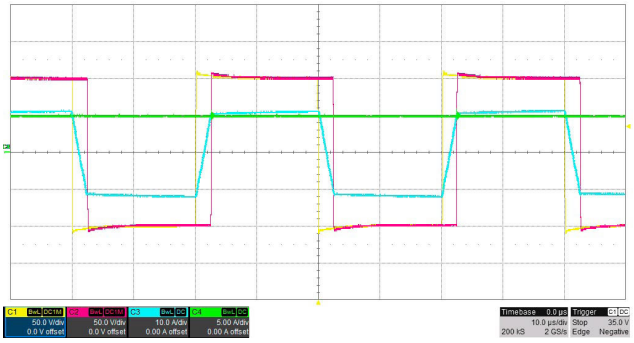

FIGURE 14. Measured converter main waveforms: $P_o = 1$ kW, $v_i = 200$ V, $v_o = 200$ V. Yellow trace: Primary side voltage v_p (50 V/div). Magenta trace: Secondary side voltage v_s (50 V/div). Blue trace: Inductor current i_L (10 A/div). Green trace: Output current i_o (5 A/div). Timescale (10 μs/div).

with the optimum value obtained in FIGURE 11. FIGURE16 compares the efficiency between the conventional phase shift method and the proposed one at different input voltage levels. The improvement in efficiency is most noticeable as the stage

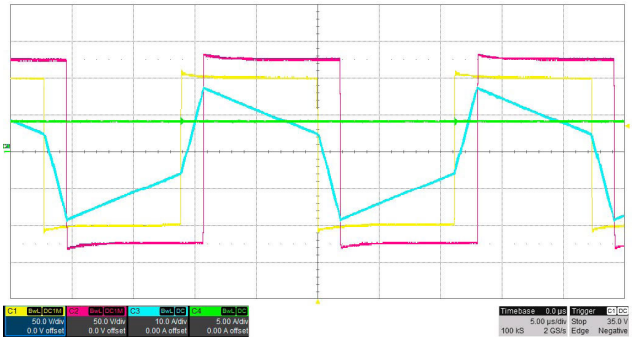

FIGURE 15. Measured converter main waveforms: $P_o = 1$ kW, $v_i = 200$ V, $v_o = 250$ V. Yellow trace: Primary side voltage v_p (50 V/div). Magenta trace: Secondary side voltage v_s (50 V/div). Blue trace: Inductor current i_L (10 A/div). Green trace: Output current i_o (5 A/div). Timescale (5 μs/div).

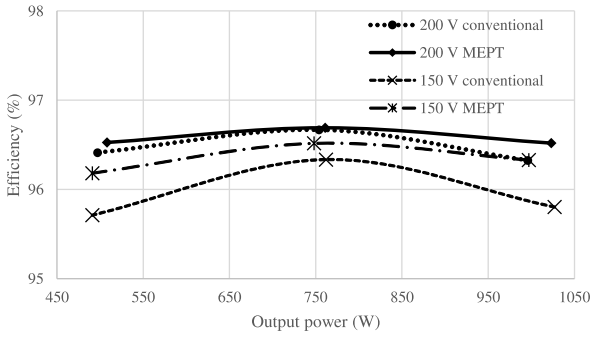

FIGURE 16. Efficiency comparative of the conventional ϕ control and the proposed MEPT control.

moves away from its optimum operating point. At the optimum voltage ratio, the proposed control presents a significant improvement over the conventional one at high currents.

V. CONCLUSION

The paper presents a novel variable frequency digital output voltage control of DAB based on a new parametric small-signal model of the converter. This model is obtained thorough the generalized state space averaged model that is performed in a complete form and applied to a half bridge configuration in order to design a digital variable frequency control. Additionally, using ϕ as control variable, a second slower control loop is added to find the point of maximum efficiency. Both simulation and experimental results agree corroborating theoretical predictions and the feasibility of the proposal. Finally, main contributions of the paper can be summarized as follows: Development of a novel analytical small-signal model that is also suitable for half bridge DAB and can be used for designing variable-frequency output voltage controllers, and efficiency improvement by means the addition of a phase shifting control loop based on a perturb and observe strategy.

REFERENCES

[1] B. Zhao, Q. Song, W. Liu, and Y. Sun, "Overview of dual-active-bridge isolated bidirectional DC–DC converter for high-frequency-link power-conversion system," *IEEE Trans. Power Electron.*, vol. 29, no. 8, pp. 4091–4106, Aug. 2014.

[2] N. Hou and Y. W. Li, "Overview and comparison of modulation and control strategies for a nonresonant single-phase dual-active-bridge DC–DC converter," *IEEE Trans. Power Electron.*, vol. 35, no. 3, pp. 3148–3172, Mar. 2020.

[3] J. Everts, F. Krismer, J. Van den Keybus, J. Driesen, and J. W. Kolar, "Optimal ZVS modulation of single-phase single-stage bidirectional DAB AC–DC converters," *IEEE Trans. Power Electron.*, vol. 29, no. 8, pp. 3954–3970, Aug. 2014.

[4] L. Xue, Z. Shen, D. Boroyevich, P. Mattavelli, and D. Diaz, "Dual active bridge-based battery charger for plug-in hybrid electric vehicle with charging current containing low frequency ripple," *IEEE Trans. Power Electron.*, vol. 30, no. 12, pp. 7299–7307, Dec. 2015.

[5] A. Taylor, G. Liu, H. Bai, A. Brown, P. M. Johnson, and M. McAmmond, "Multiple-phase-shift control for a dual active bridge to secure zero-voltage switching and enhance light-load performance," *IEEE Trans. Power Electron.*, vol. 33, no. 6, pp. 4584–4588, Jun. 2018.

[6] M. Roche, W. Shabbir, and S. A. Evangelou, "Voltage control for enhanced power electronic efficiency in series hybrid electric vehicles," *IEEE Trans. Veh. Technol.*, vol. 66, no. 5, pp. 3645–3658, May 2017.

[7] H. Vu Nguyen, D.-D. To, and D.-C. Lee, "Onboard battery chargers for plug-in electric vehicles with dual functional circuit for low-voltage battery charging and active power decoupling," *IEEE Access*, vol. 6, pp. 70212–70222, 2018.

[8] N. M. L. Tan, T. Abe, and H. Akagi, "Design and performance of a bidirectional isolated DC–DC converter for a battery energy storage system," *IEEE Trans. Power Electron.*, vol. 27, no. 3, pp. 1237–1248, Mar. 2012.

[9] F. Xue, R. Yu, and A. Q. Huang, "A 98.3% efficient GaN isolated bidirectional DC–DC converter for DC microgrid energy storage system applications," *IEEE Trans. Ind. Electron.*, vol. 64, no. 11, pp. 9094–9103, Nov. 2017.

[10] X. Liu, H. Li, and Z. Wang, "A fuel cell power conditioning system with low-frequency ripple-free input current using a control-oriented power pulsation decoupling strategy," *IEEE Trans. Power Electron.*, vol. 29, no. 1, pp. 159–169, Jan. 2014.

[11] S. Shao, H. Chen, X. Wu, J. Zhang, and K. Sheng, "Circulating current and ZVS-on of a dual active bridge DC-DC converter: A review," *IEEE Access*, vol. 7, pp. 50561–50572, 2019.

[12] A. Tong, L. Hang, G. Li, X. Jiang, and S. Gao, "Modeling and analysis of a dual-active-bridge-isolated bidirectional DC/DC converter to minimize RMS current with whole operating range," *IEEE Trans. Power Electron.*, vol. 33, no. 6, pp. 5302–5316, Jun. 2018.

[13] F. Krismer and J. W. Kolar, "Closed form solution for minimum conduction loss modulation of DAB converters," *IEEE Trans. Power Electron.*, vol. 27, no. 1, pp. 174–188, Jan. 2012.

[14] F. Krismer, J. Biela, and J. W. Kolar, "A comparative evaluation of isolated bi-directional DC/DC converters with wide input and output voltage range," in *Proc. 40th IAS Annu. Meeting Conf. Rec. Ind. Appl. Conf.*, vol. 1, Oct. 2005, pp. 599–606.

[15] H. Qin and J. W. Kimball, "Generalized average modeling of dual active bridge DC–DC converter," *IEEE Trans. Power Electron.*, vol. 27, no. 4, pp. 2078–2084, Apr. 2012.

[16] A. Davoudi and J. Jatskevich, "Realization of parasitics in state-space average-value modeling of PWM DC-DC converters," *IEEE Trans. Power Electron.*, vol. 21, no. 4, pp. 1142–1147, Jul. 2006.

[17] S. R. Sanders, J. M. Noworolski, X. Z. Liu, and G. C. Verghese, "Generalized averaging method for power conversion circuits," *IEEE Trans. Power Electron.*, vol. 6, no. 2, pp. 251–259, Apr. 1991.

[18] U. Javaid and D. Dujic, "Arbitrary order generalized state space average modeling of switching converters," in *Proc. IEEE Energy Convers. Congr. Expo. (ECCE)*, Sep. 2015, pp. 6399–6406.

[19] G. G. Oggier, G. O. García, and A. R. Oliva, "Modulation strategy to operate the dual active bridge DC-DC converter under soft switching in the whole operating range," *IEEE Trans. Power Electron.*, vol. 26, no. 4, pp. 1228–1236, Apr. 2011.

[20] F. Krismer and J. W. Kolar, "Accurate power loss model derivation of a high-current dual active bridge converter for an automotive application," *IEEE Trans. Ind. Electron.*, vol. 57, no. 3, pp. 881–891, Mar. 2010.

[21] H. M. El-Helw, A. Magdy, and M. I. Marei, "A hybrid maximum power point tracking technique for partially shaded photovoltaic arrays," *IEEE Access*, vol. 5, pp. 11900–11908, 2017.

[22] S.-C. Wang, H.-Y. Pai, G.-J. Chen, and Y.-H. Liu, "A fast and efficient maximum power tracking combining simplified state estimation with adaptive perturb and observe," *IEEE Access*, vol. 8, pp. 155319–155328, 2020.

[23] M. Kasper, R. M. Burkart, G. Deboy, and J. W. Kolar, "ZVS of power MOSFETs revisited," *IEEE Trans. Power Electron.*, vol. 31, no. 12, pp. 8063–8067, Dec. 2016.

IVAN RUIZ ERNI (Graduate Student Member, IEEE) was born in Spain. He received the bachelor's degree in electronic and automatic engineering and the master's degree in electronics from the University of Saragossa, Spain, in 2014 and 2015, respectively.

He currently combines his work in private companies within the automotive industry while pursuing the Ph.D. degree in electronics from Universitat Rovira i Virgili. His research interests include power electronics converters and its control for electrical vehicles.

ENRIC VIDAL-IDIARTE (Member, IEEE) received the Licenciado en Informática and Ph.D. degrees from the Universitat Politècnica de Catalunya, Barcelona, Spain, in 1993 and 2001, respectively.

He is currently an Associate Professor with the Departament d'Enginyeria Electrònica, Elèctrica i Automàtica, Escola Tècnica Superior d'Enginyeria, Universitat Rovira i Virgili, Tarragona, Spain, where he is working in the field of digital and robust control of power converters. He is also a member of the Grup d'Automàtica i Electrònica Industrial (GAEI). His research interests include power conditioning for vehicles, satellites, and renewable energy.

JAVIER CALVENTE (Member, IEEE) received the Ingeniero de Telecomunicación and Ph.D. degrees from the Universitat Politècnica de Catalunya (UPC), Barcelona, Spain, in 1994 and 2001, respectively.

He was a Visiting Scholar with Alcatel Space Industries, Toulouse, France, in 1998. Since 2003, he has been an Associate Professor with the Departament d'Enginyeria Electrònica, Elèctrica i Automàtica, Universitat Rovira i Virgili (URV), Tarragona, Spain, where he has been involving in the fields of power electronics and control systems. In 2019, he was a Visiting Associate Professor with The University of British Columbia (UBC), Vancouver, BC, Canada. He is also a member of the Grup d'Automàtica i Electrònica Industrial (GAEI), Tarragona.

LUIS GUASCH-PESQUER was born in Tarragona, Spain, in 1964. He received the B.S. degree in industrial engineering and the Ph.D. degree in engineering from the Universitat Politècnica de Catalunya, Barcelona, Spain, in 1996 and 2006, respectively.

He is currently an Associate Professor with the Departament d'Enginyeria Electrònica, Elèctrica i Automàtica, Universitat Rovira i Virgili, Tarragona. His research interests include electric machines and power system quality.